Comparison of empirical potentials for calculating structural properties of amorphous carbon films by molecular dynamics simulation

Xiaowei Li[a,b], Aiying Wang[b], Kwang-Ryeol Lee[a,*]

[a] Computational Science Center, Korea Institute of Science and Technology, Seoul 136-791, Republic of Korea
[b] Key Laboratory of Marine Materials and Related Technologies, Zhejiang Key Laboratory of Marine Materials and Protective Technologies, Ningbo Institute of Materials Technology and Engineering, Chinese Academy of Sciences, Ningbo 315201, PR China

ARTICLE INFO

ABSTRACT

Amorphous carbon (a-C) films were deposited by molecular dynamics simulation using Tersoff, REBO and AIREBO potentials, respectively. The hybridization and the distributions of both bond angles and lengths as a function of the three potentials were analyzed, and the density and residual stress were calculated. Results revealed that comparing with the Tersoff and REBO potentials, the AIREBO potential gave the more reasonable values of density, hybridization ratio and residual stress. This attributed to that in AIREBO potential, the conjugation effect between the different coordinated atoms was corrected by revising the bond order term, which was responsible for the sp^3 content; while the introduction of long-range Lennard-Jones (LJ) interaction described the compressed graphite structure correctly following the rational density; in particular, both the LJ and torsion interactions were indispensable for the accurate evaluation of residual stress of a-C films. In addition, the simulation result using AIREBO potential suggested no dependence on the processing methods of atom-by-atom deposition and liquid-quenching method.

1. Introduction

Amorphous carbon (a-C) film has been widely used in the fields of automobile, aerospace, biomedicine and so on due to its superior mechanical, tribological, optical properties and chemical inertness [1–3]. Because the excellent properties of a-C film originate from its special structure composed of sp^3 and sp^2 hybridizations, the accurate evaluation for sp^3/sp^2 structures is essential for systematic exploration of its properties. However, due to the difficulties in quantitative analysis of the atomic structure by experiment, such as Raman [4], X-ray photoelectron spectroscopy [5], electron energy loss spectroscopy [6] and nuclear magnetic resonance [7], it is only possible to obtain an insufficient or a phenomenal understanding of the relationship between the structure and properties.

Molecular dynamic (MD) simulation either of *ab initio* or empirical method enables one to capture deeper insight on the structure-property relationship from atomic or electronic scale. In principle, a*b initio* MD simulation is applicable to a-C system to obtain an accurate description of the structure and properties [8,9]. However, high computational expense practically limits the application to a small system composed of less than 100 atoms. It would be too expensive to simulate the growth process of a-C film. On the other hand, the simulation with empirical potential describes the relationship between the energy and geometry with a set of relatively simple potential functions, which allows it to be applied to much larger systems than *ab initio* MD simulation. Empirical MD simulations have been successful in simulating the growth behavior of a-C film and describing the structure-property relationship. For example, Li et al. [10] carried out MD simulation of a-C film growth to investigate the structural evolution for various incident energies of carbon atoms. They revealed the "Point-Line-Net" formation process. Stuart et al. [11] simulated the a-C films with different densities and reported that the structural factors such as void volumes and coordination numbers were more useful than ring size distributions in characterizing the structure of a-C film. Ma et al. [12] studied the microscopic process underlying the friction of a-C films using MD simulation, and revealed that the excellent lubricity of a-C arose from the atomic shear induced by strain localization.

In the empirical MD simulation, the reliable description of interatomic interactions is strongly and solely dependent on the empirically interatomic potential. The selection of empirical potential is thus crucial for accurate simulation of the a-C model. It would affect the hybridized bond structure and the corresponding properties. Many empirical potential models are now available for carbon system, including Tersoff [13,14], REBO [15], AIREBO [16], Reactive Force Field

---

potential [17], Environment Dependent Interaction potential [18] and Charge optimized many-body potential [19]. Among of them, Tersoff, REBO and AIREBO potentials have been more widely used to study the structural properties of a-C film [10–12,20,21], but it is yet to be obvious that how much the different potentials result in the difference in the simulated structures and which factor in the potential model mainly causes the difference in the simulated results. In the present work, we performed the same a-C film growth simulation with different empirical potentials of Tersoff [14], REBO [15] and AIREBO [16] to comparatively address the dependence of simulated result on the empirical potentials model. The density, hybridization structure, residual stress and both the bond angle and bond length distributions were analyzed. The results evidently showed that the AIREBO potential correctly handled the overbinding effect of specific bonding configurations. Furthermore, AIREBO potential led to the reasonable description of structure and properties owing to the additional long-range Lennard-Jones (LJ) and torsion interaction terms.

2. Simulation details

Classical MD simulation was used to carry out the comparative study of the empirical potentials of carbon. We compared the structural properties of a-C films prepared by the identical deposition simulation using three different interatomic potentials (Tersoff, REBO, and AIREBO potentials). Fig. 1 gave the model used in the calculations according to previous studies [20,21]. A diamond (0 0 1) single crystal with size of $20.18 \times 20.18 \times 25 \, Å^3$ in x, y and z directions was served as substrate, which consisted of 29 atomic layers with 64 carbon atoms per layer and was equilibrated at 300 K for 100 ps before carbon deposition simulation. The atoms in the bottom three monolayers were fixed to mimic the bulk substrate. Temperature of the next eight layers was kept at 300 K during simulation for providing a thermal reservoir to the simulation system. Atoms of top eighteen layers were totally unconstrained to simulate the structural evolution during deposition. The incident carbon atoms were introduced at the position of 50 Å above the substrate surface at a random {x, y} position. The deposition was simulated using *NVE* ensemble implemented in the large-scale atomic/
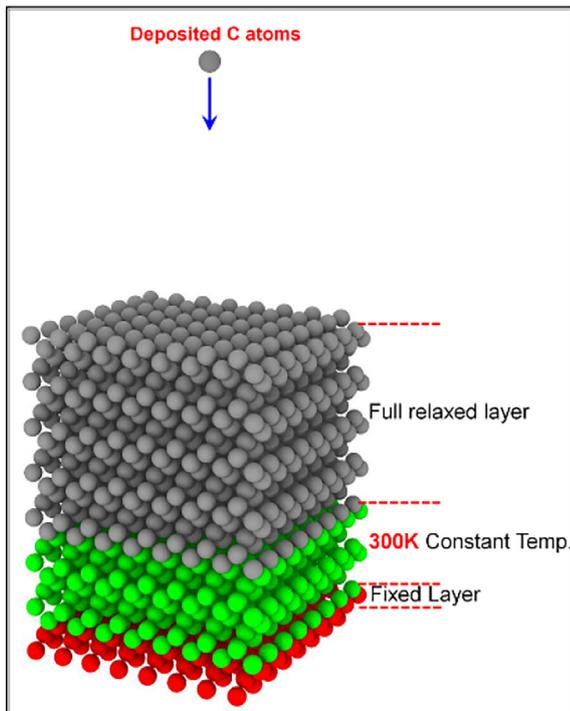

Fig. 1. Deposition model used in the calculations.

molecular massively parallel simulator (LAMMPS) code [22]. Periodic boundary conditions were applied in both the x and y directions.

Total 1750 carbon atoms were deposited at the normal incident angle. The time step of simulation was 0.25 fs. The kinetic energy of incident carbon atoms was fixed at 70 eV/atom, that was known to be the optimum energy for a highly stressed and dense tetrahedral amorphous carbon film deposition [10]. The time interval between the sequential carbon atom depositions was 10 ps, which corresponded to an ion flux of $2.46 \times 10^{28} /m^2 s$. The previous report has indicated that the time interval of 10 ps was enough for relaxing the atomic structure induced by the energetic incident carbon bombardment [10]. Diffusion or rearrangement processes were ignored in this simulation, because the event would be very rare at room temperature once the structural agitation by energetic carbon bombardment was settled down. The system temperature was rescaled to 300 K by the Berendsen method [23] after 10 ps when the atomic arrangement caused by the bombardment of the incident atoms was finished. Heat bath coupling constant was set to be 10 fs in all simulations.

3. Results and discussion

3.1. Results

Fig. 2 shows the morphologies of deposited films obtained by Tersoff, REBO and AIREBO potentials. Color of atoms represents the coordination number. The amorphous carbon films with the thickness about 36 Å is obtained for each case. Since the incident energy of carbon atoms (70 eV) is much higher than the cohesive energy of diamond (7.6–7.7 eV/atom) [21], the incident C atoms can penetrate into the diamond substrate, resulting in the intermix layer with high residual stress due to impairing the regular lattice of substrate. After intermixing, a steady state film grows with the surface transition layer.

This growth behavior is evident when analyzing the thickness dependence of film properties. Fig. 3 shows the variations of density and coordination number along the growth direction. The coordination number of carbon atoms is determined by using a cutoff value in the interatomic distance of 1.85 Å. It reveals that the a-C film can be divided into three regions: interfacial intermixing region, steady state growth region and surface transition region. The structural property gradient can be observed obviously in the intermixing region (yellow region in Fig. 3), which is caused by the intermixing with the substrate. The surface transition region (gray region in Fig. 3) exhibits a markedly deterioration of the structure and properties. In the steady state growth region with the thickness about 20 Å, the constant values for density and coordination numbers are obtained along the growth direction (light blue region in Fig. 3). The steady state growth region is used for further analysis of the structural properties of the deposited films using different interatomic potentials.

Fig. 4 shows the density, hybridization ratios of the bonds, and the residual stress of a-C films obtained by the three interatomic potentials. The biaxial stress, σ, in the film is calculated using Eqs. (1)–(3).

$$P_{IJ} = \frac{\sum_k^N m_k v_{kI} v_{kJ}}{V} + \frac{\sum_k^N r_{kI} f_{kJ}}{V} \tag{1}$$

$$P = \frac{P_{xx} + P_{yy} + P_{zz}}{3} \tag{2}$$

$$\sigma = -\frac{3}{2} P \tag{3}$$

Here, I and J take on values x, y and z; k is the atom in the domain; N is the number of atoms in the system; m_k is the mass of atom k; v_{kI} and v_{kJ} are the Ith and Jth components of the velocity of atom k; V is the system volume (or area in 2d); r_{kI} is the Ith component of the position of atom k; f_{kJ} is the Jth component of the force applied on atom k; P is the hydrostatic pressure; P_{xx}, P_{yy} and P_{zz} are the diagonal components of
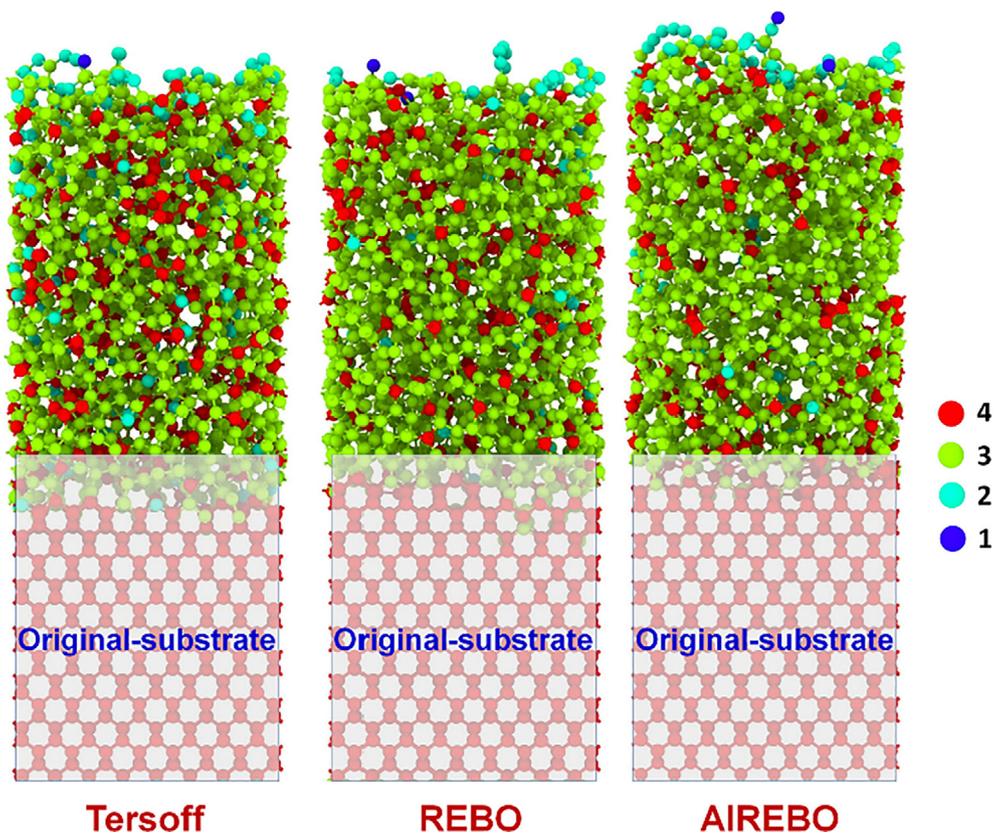
Fig. 2. Final morphologies of deposited films obtained by Tersoff, REBO and AIREBO potentials, respectively. The dark blue, light blue, green and red colors correspond to 1, 2, 3 and 4-fold coordinated C atoms separately.
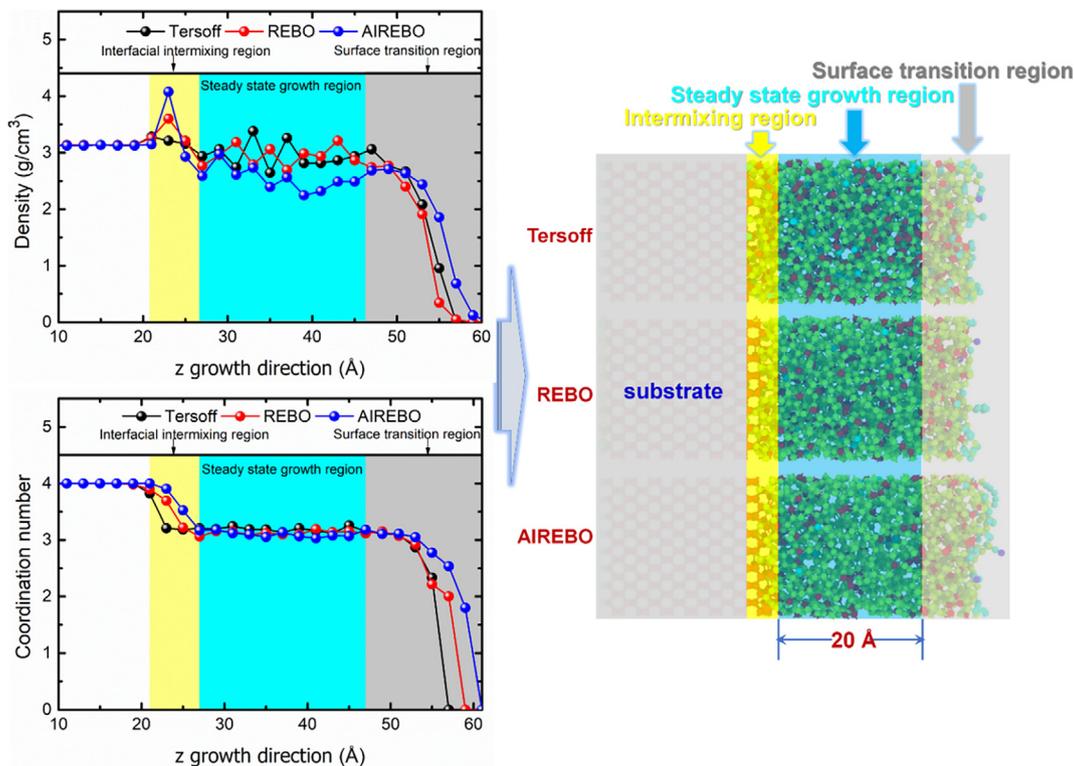

Fig. 3. Thickness dependence of density and coordination number for the films obtained by Tersoff, REBO and AIREBO potentials, respectively.
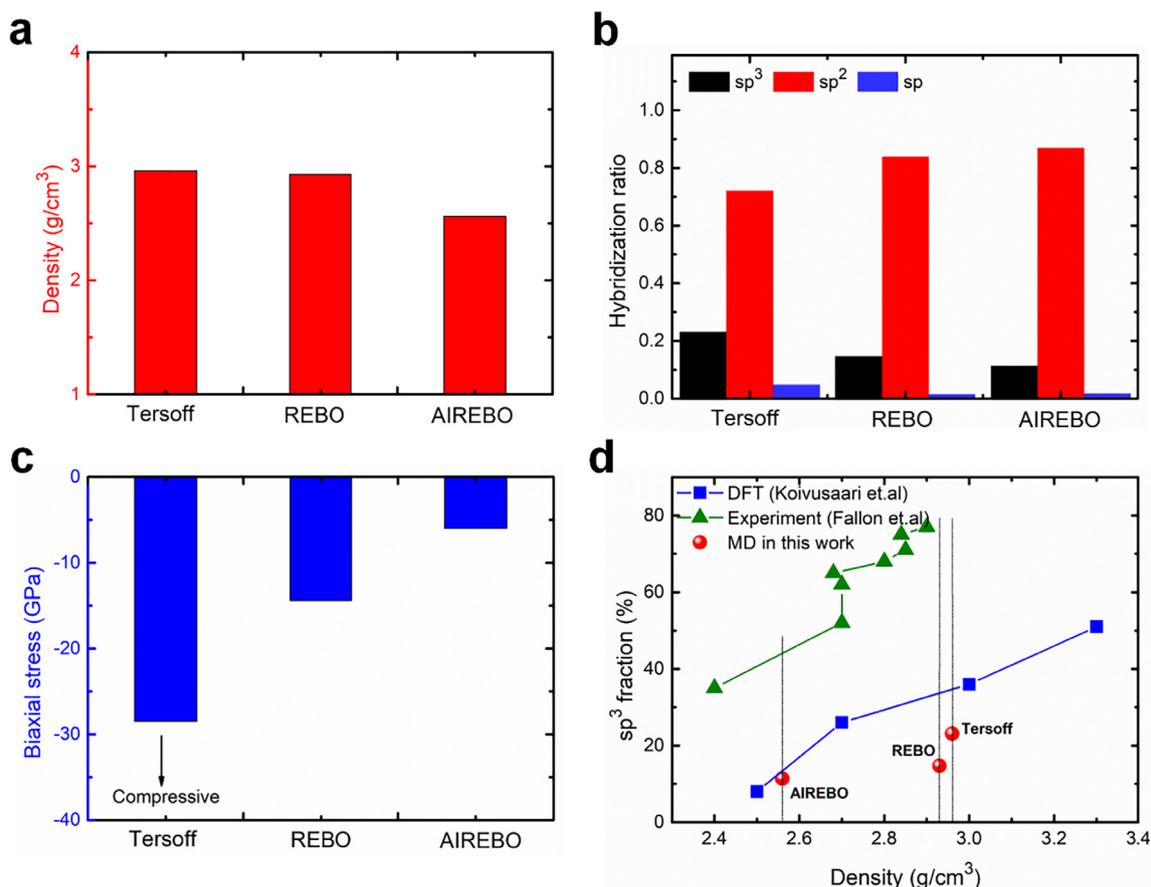
Fig. 4. (a) Density, (b) hybridization ratios (sp^3, sp^2, sp) and (c) residual stress of deposited films obtained by Tersoff, REBO and AIREBO potentials, respectively. (d) Comparison of the sp^3 fraction obtained in the present work with the experimental result by Fallon et al. [26] and the DFT simulation result by Koivusaari et al. [27].

the stress tensor. The first term of Eq. (1) is the kinetic energy tensor and the second term uses components of the virial tensor as the sum of pair, bond, angle, dihedral, improper and kspace (long-range coulombic interaction) contributions, which includes all terms except the kinetic energy. The pressure, P, is converted to the biaxial stress by multiplying the pressure by a factor of 1.5, according to the method of McKenzie [24,25].

Fig. 4a shows that the density varies from 2.96 to 2.93 to 2.56 g/cm^3 as the interatomic potential changes from Tersoff to REBO and AIREBO potentials, respectively. Bond hybridization obtained from the co-ordination number is also significantly varied by the interatomic potentials as shown in Fig. 4b: sp^3 bond fraction decreases from 23.1, 14.6 to 11.4% with contrasting increase in the sp^2 bond fraction. The structural change is associated with the decrease in the residual compressive stress as the interatomic potential changes from Tersoff (28.5 GPa), REBO (14.4 GPa) to AIREBO (6.0 GPa) (Fig. 4c). Fig. 4d shows the comparison of sp^3 fraction in the present work with the experimental result by Fallon et al. [26] and the DFT simulation result by Koivusaari et al. [27]. Both the *ab initio* simulation and present empirical simulation result in lower values than the experimentally reported values. It must be noted that there remain arguments about the experimental quantification of the sp^3 bond fraction based on some hypothetical spectroscopic analysis [28,29]. It would be interesting that the sp^3 fraction obtained by the present simulations using AIREBO potential is in good agreement with that of the *ab initio* simulations where the a-C film was obtained by the melting and quenching method. In contrast, the results of Tersoff and REBO potentials are significantly different from those of the *ab initio* simulation results. In addition, noted that the residual stress obtained by using AIREBO potential is more consistent with the experimental measurements, where the compressive
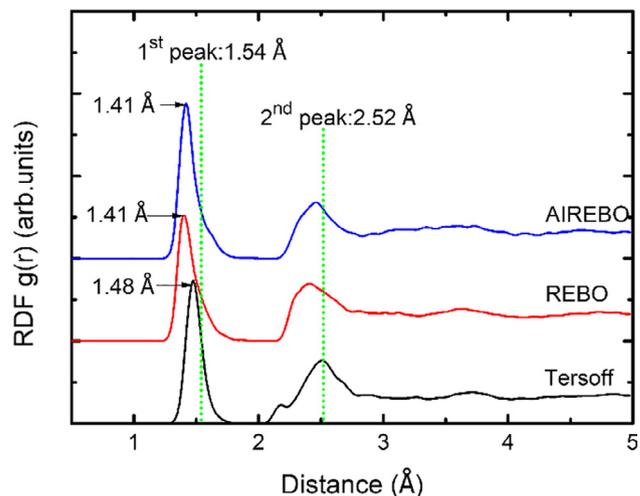
residual stress ranged from 5 to 10 GPa for the tetrahedral a-C films [30].

Radial distribution functions, $g(r)$, given by Eq. (4) are presented in Fig. 5 to find the variation of atomic bond structure according to the used interatomic potentials.

$$g(r) = \frac{dN}{\rho \cdot 4\pi r^2 dr} \tag{4}$$

where ρ is the average density of system, dN is the number of atoms

Fig. 5. Radial distribution functions of a-C films obtained by Tersoff, REBO and AIREBO potentials, respectively.
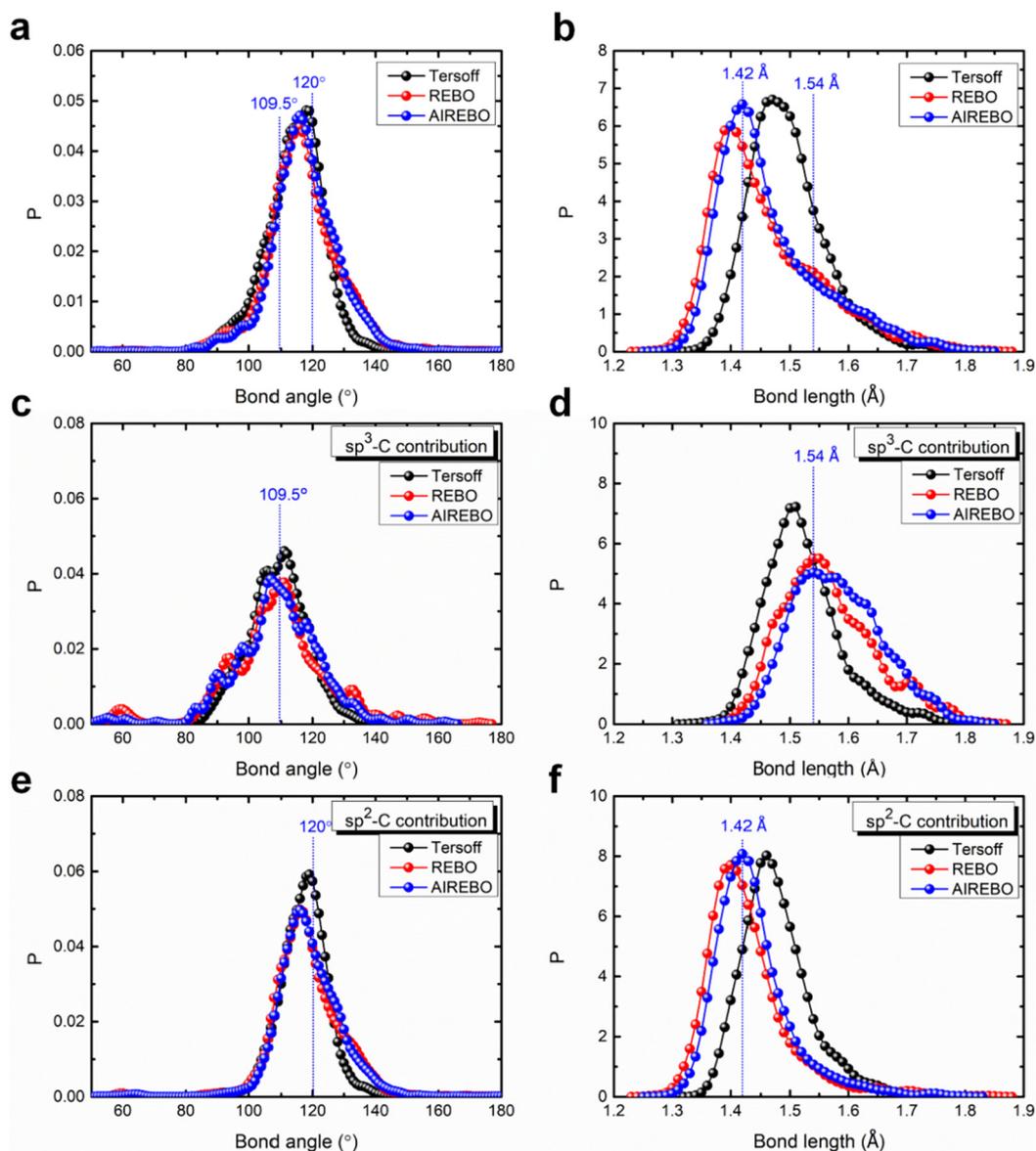
Fig. 6. Bond angle and length distributions for the films obtained by Tersoff, REBO and AIREBO potentials, respectively, in which (a) and (b) are total bond angle and length distributions; (c) and (e) are the bond angle distributions from only sp^3 C or sp^2 C, respectively; (d) and (f) are the bond length distributions from only sp^3 C or sp^2 C, respectively.

from r to $r + dr$. All RDF functions exhibit the long-range disorder with short-range order, which is the typical character of amorphous structure. The 1st and 2nd nearest neighbor peaks of diamond are respectively located at 1.54 and 2.52 Å separately [10], as indicated by the green vertical lines. In the simulated a-C films, the 1st nearest peak position changes from 1.48 to 1.41 Å as the Tersoff, REBO and AIREBO potentials are used. Second nearest peak position shows similar behavior depending on the used interatomic potentials. The change in the bond length (the 1st nearest peak position) should be related to the hybridization of atomic bonds. On the other hand, the 2nd nearest peak position is dependent on both the bond lengths and bond angles.

For more details in changes of the bond angle and bond length, we analyze the distributions of the bond angles and bond lengths for each interatomic potential, as illustrated in Fig. 6. The equilibrium bond angles and bond lengths of diamond (109.5°, 1.42 Å, respectively) and graphite (120°, 1.54 Å, respectively) are also presented as the blue vertical lines. The total bond angle distributions shown in Fig. 6a are little dependent on the interatomic potential. However, the total bond length distribution shown in Fig. 6b shifts to the smaller bond length

when REBO or AIREBO potentials are used. These results are consistent with the RDF in Fig. 5. The contribution of sp^3 C or sp^2 C bonds to the bond angle and bond length distributions is further explored, as illustrated in Fig. 6c–f. It is evident in Fig. 6c and 6e that the bond angle distribution of sp^3 C corresponds to that of the diamond for each case, while that of the sp^2 C shows a slight down-shift from that of graphite. This behavior is almost independent of the interatomic potential used in this work. This shift would result from the puckered hexagonal six carbon rings or the formation of the rings of carbon atoms less than six.

Fig. 6d and 6f show the bond length distributions of sp^3 C and sp^2 C, respectively. The bond length distributions of sp^3 C modeled by the REBO and AIREBO potentials coincides with that of diamond, while the distribution modeled by the Tersoff potential shifts significantly downward. Different behavior is also observed in the bond length distribution of sp^2 C (Fig. 6f). The bond length distribution of sp^2 C for AIREBO potential is consistent with that of graphite, while that for Tersoff potential shifts upward and it shifts downward for REBO potential. By comparison of the bond structure, it can be deduced that the AIREBO potential can describe the sp^3 C and sp^2 C structures more

accurate than Tersoff and REBO potentials. In particular, this analysis exhibits the structural origin of the different residual stress of a-C film. Residual stress of the simulated film using AIREBO potential originates from both the distorted bond angles and bond lengths of sp^3 C and sp^2 C bonds. When using REBO potential, the further decrease in bond lengths of sp^3 C and sp^2 C bonds would be additionally considered resulting in the higher value of residual compressive stress (see Fig. 4c). In the case of using Tersoff potential, the significant decrease in the bond lengths of sp^3 C shown in Fig. 6d would be considered as the major reason for the compressive stress. Since the experimentally measured residual stress is more consistent with that using AIREBO potential, one would consider the bond structure distortion as the physically acceptable origin of the compressive stress.

3.2. Discussion

All three potentials (Tersoff, REBO and AIREBO) are based on the bond-order formalism by Abell [31]. In the Tersoff potential, the binding energy of the system is presented as the sum of nearest-neighbor pairwise interactions. The basic formulas for Tersoff potential are as following [14].

$$E = \sum_{i>j} f_c(r_{ij}) \left[V_R(r_{ij}) - \frac{b_{ij+b_{ji}}}{2} V_A(r_{ij}) \right] \tag{5}$$

$$\overline{b_{ij}} = \frac{1}{2}[b_{ij} + b_{ji}] \tag{6}$$

where E is the total energy of the system; the indices i and j run over the atoms of the system; r_{ij} is the distance from atom i to atom j. V_R and V_A represent repulsive and attractive potentials, respectively. f_c is a smooth cutoff function, limiting the effective range of the potential. b_{ij} is the bond order term, which depends on both the coordination of the atoms and the bond angle between the atoms i, j, and k. Although the Tersoff potential describes C—C bond lengths and energies reasonably well, it only takes into account the nearest-neighbor interaction and overestimates the binding energy (named "overbinding") for intermediate bonding configurations, such as the bonding between a three-coordinated C atom and a four-coordinated C atom.

In REBO potential, such conjugated effects or many-body interactions from Tersoff potential are taken into account by means of bond order function as following [15].

$$\overline{b_{ij}} = \frac{1}{2}[b_{ij}^{\sigma-\pi} + b_{ji}^{\sigma-\pi}] + b_{ij}^{\pi} \tag{7}$$

where the values for the functions $b_{ij}^{\sigma-\pi}$ and $b_{ji}^{\sigma-\pi}$ depend on the local coordination and bond angles for atoms i and j, respectively. The additional function b_{ij}^{π} is the overbinding correction term for bonds between pairs of atoms that have different coordination, which can be further written as a sum of two terms:

$$b_{ij}^{\pi} = \sum_{ij}^{RC} + b_{ij}^{DH} \tag{8}$$

where the first term Π_{ij}^{RC} depends on whether a bond between the atoms i and j has radical character and is part of a conjugated system. The second term b_{ij}^{DH} depends on the dihedral angle for carbon–carbon double bonds. So, compared with Tersoff potential, the effects from the coordination, bond angle and conjugation are all considered in the bond order term of REBO potential. However, the REBO potential also describes only the short-range interactions as the Tersoff potential, making it poorly suited for system with significant intermolecular interaction. In addition, the REBO potential also has no torsional potential for hindered rotation about single bond, reflecting its original focus on the network solids such as diamond and small molecular fragments.

To overcome the limitations of REBO potential, the AIREBO potential is introduced by Stuart et al. [16], in which two additional energy terms besides the REBO interaction for covalent bonding are included: one is the Lennard-Jones (LJ) 12–6 potential, E^{LJ}, that represents the van der Waals dispersion interactions for nonbonded long-range intermolecular interactions, and the other is torsion potential, E^{tors}, which describes various dihedral angles coupled with single bonds. The detailed information of the potential is presented as below [16].

$$E = \frac{1}{2} \sum_i \sum_{j \neq i} \left(E_{ij}^{REBO} + E_{ij}^{LJ} + \sum_{k \neq i,j} \sum_{l \neq i,j,k} E_{kijl}^{tors} \right) \tag{9}$$

In this potential, the barrier formed by the steep repulsion wall of E^{LJ} term prevents the nonbonded atom from approaching close enough to interact via the REBO potential, while the E^{tors} term could correctly predict a barrier to rotation about homogeneously substituted sp^3-sp^3 bonds.

The REBO potential originates from the Brenner potential [32]. Jäger et al. [33] reported that when the overbinding correction was switched off in the Brenner potential, the obtained sp^3 fraction was similar to that by Tersoff potential, otherwise it was lower than that by the Tersoff potential. It can be concluded that when using the Tersoff potential, the higher sp^3 fraction of about 23.1% mainly results from the particular potential energy term overestimating the pair interaction between the different coordinated C atoms, while the REBO and AIREBO potentials manage this overbinding accurately, resulting in the lower sp^3 bond fraction (see Fig. 4b).

Fig. 4a shows that the densities in the films by the Tersoff and REBO potentials are similar (2.96 and 2.93 g/cm^3 respectively), which are higher than 2.56 g/cm^3 by the AIREBO potential. The Tersoff and REBO potentials describe the covalent bonding within a distance of 2.15 and 2.25 Å, respectively. However, these potentials do not include the long-range van der Waals interaction between the separate planes of graphite and there is also no energy penalty for nonbonded π interactions. Hence, too many intermolecular pairs are located at close distance and compressed graphite structures are generated, leading to the unphysical high densities close to that of diamond. This is also confirmed by previous study [33,34]. In contrast, the AIREBO potential describes the van der Waals interactions ranging from 2.25 to 10.2 Å, which can model the interactions between the graphite-like structures. Lower density values in Fig. 4a would result from considering these long-range interactions.

The effects of two additional terms (LJ and torsion term) in the AIREBO potential shown in Eq. (9) are further investigated. We perform the same simulation with AIREBO potentials with only LJ or torsion term to consider the effect of each term separately on the structural properties. Fig. 7a and b show the density and residual stress of the simulated a-C films using only LJ or torsion term in the AIREBO potential, respectively. For comparison, the result using original AIREBO potential with both LJ and torsion terms is also reproduced. When using the AIREBO potential with only LJ term, the density is 2.70 g/cm^3, which is similar to that obtained with original AIREBO potential (2.56 g/cm^3). In contrast, density of the simulated a-C film using the AIREBO potential with only torsion term (2.91 g/cm^3) is comparable to that by Tersoff (2.96 g/cm^3) or REBO potential (2.93 g/cm^3). This result shows that the film density is quite sensitive to the van der Waals interaction in the a-C film. Residual compressive stress is estimated too high when using the AIREBO potentials either with only LJ term or with only torsion term (Fig. 7b). This attributes to that when only torsion term is considered in AIREBO potential, the high residual stress results from the compressed graphite structure due to the lack of long-range interaction. On the contrary, when only LJ term is used, the unreal high residual stress is also followed because the absence of torsional term cannot correctly predict the barrier to rotation, such as sp^3-sp^3 bonds, inducing the high angle-bending forces. Hence, the compressive residual stress becomes comparable to the experimentally measured value, only when both LJ and torsion term are included in the interatomic potential simultaneously.
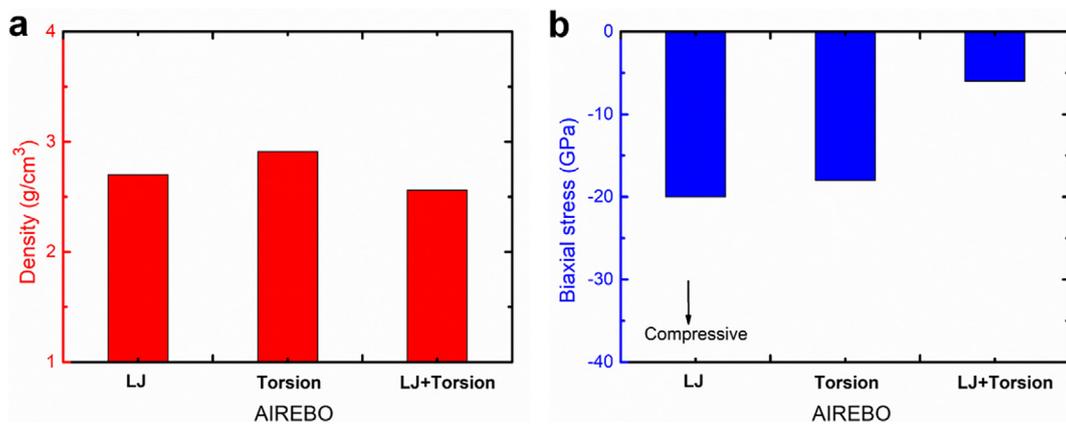
Fig. 7. The contributions of LJ or torsion terms in AIREBO potential to (a) density and (b) residual stress of a-C film.
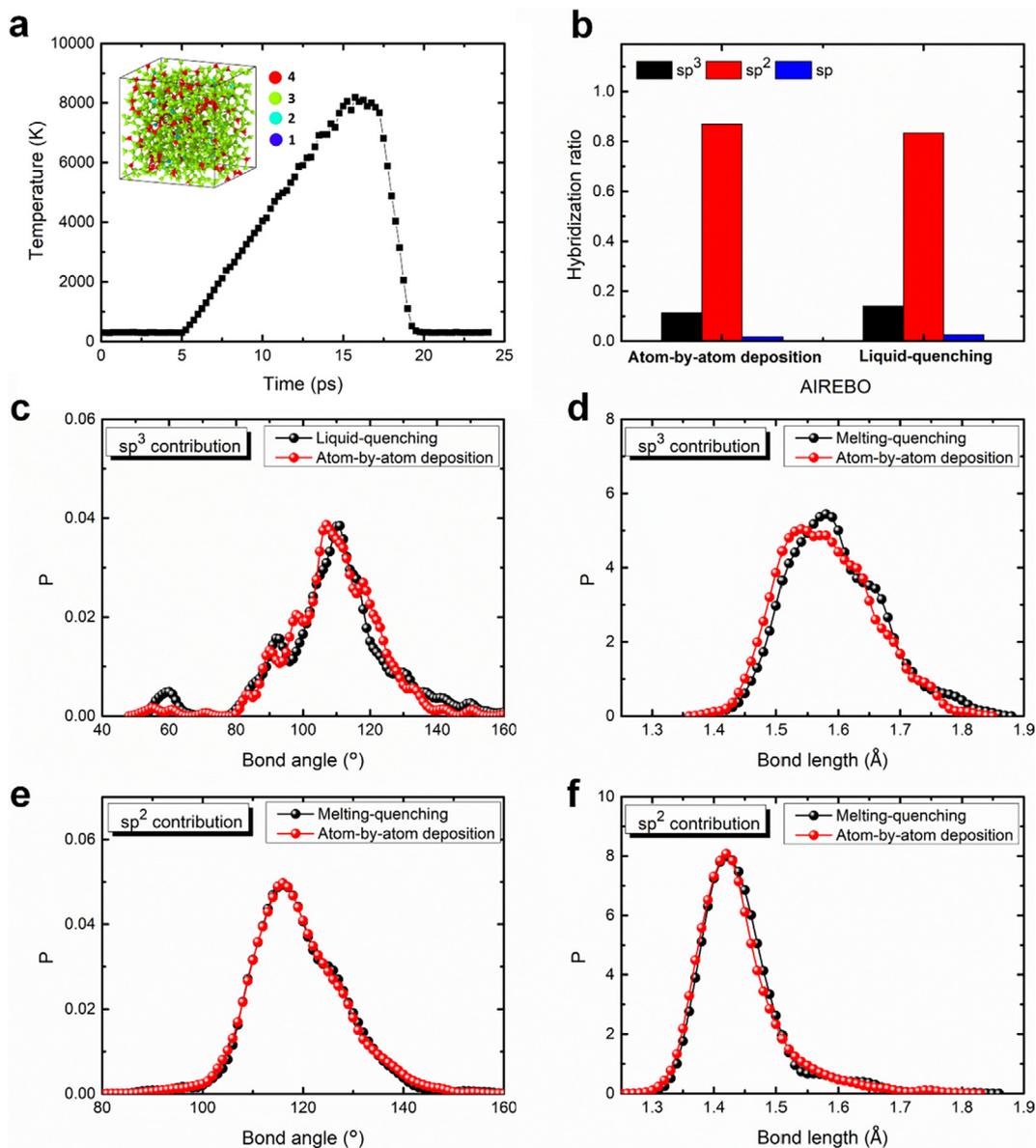

Fig. 8. Calculation result of a-C film using liquid-quenching method by MD simulation with AIREBO potential.
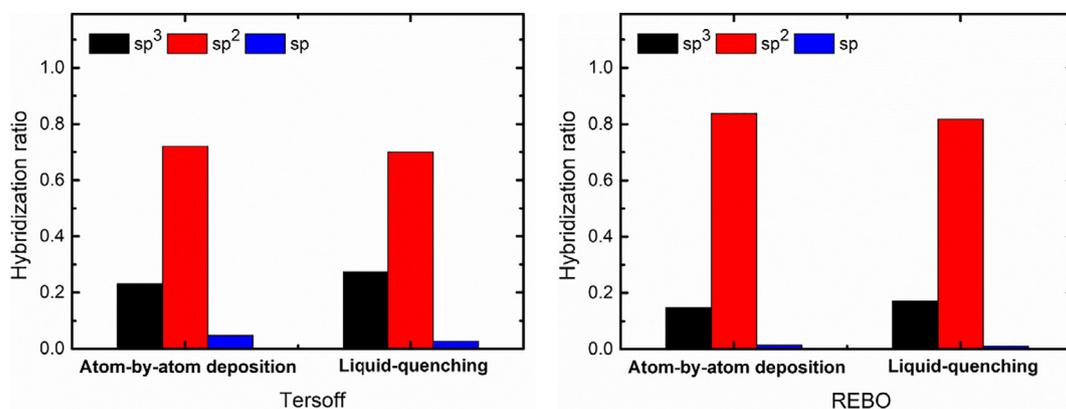
Fig. 9. Hybridization structure of a-C film using liquid-quenching method by MD simulation with Tersoff and REBO potentials, respectively.

The amorphous carbon film has been also modeled by 'liquid-quenching' simulation with predefined density value [8,9,27,34]. We further compare the liquid-quenching simulation method using AIREBO potential with that of atom-by-atom deposition method. As in the previous work [34], the initial configuration contained 1000 atoms randomly distributed with the predefined density of 2.56 g/cm^3 in a cubic simulation box of size of 19.85 × 19.85 × 19.85 Å^3. The sample was first equilibrated at 300 K for 5 ps using *NVE* ensemble with the Berendsen thermostat [23] for temperature-control and a time step of 0.25 fs; then, the sample was heated up to 8000 K and maintained for 2 ps to make complete liquid state. The liquid sample was quenched from 8000 to 300 K at the cooling rate of 3.9 × 10^{15} K/s, followed by the structure relaxation for 5 ps at 300 K. The inset in Fig. 8a shows the final structure of a-C film obtained by liquid-quenching method. The structure analysis reveals that the a-C film simulated by the liquid-quenching method is comparable with that simulated by the atom-by-atom deposition simulation, in terms of the hybridized atomic bond configuration (Fig. 8b) and the distributions of both the bond angles (Fig. 8c and e) and bond lengths (Fig. 8d and f). This result shows that using the AIREBO potential, the simulated a-C structure has no obvious dependence on the simulation methods of the a-C structure. When the Tersoff or REBO potential is adopted separately, the method-independent behavior is also observed, as illustrated in Fig. 9. In addition, the comparative result between these three different potentials, which is obtained from liquid-quenching method, is also consistent with that from the atom-by-atom deposition method.

4. Conclusions

In this work, we fabricated the a-C films by atom-by-atom deposition method using MD simulation with Tersoff, REBO and AIREBO potentials. By comparative study for the effect of different empirical potentials on the structure and properties of a-C films, it could conclude that:

(1) Density, sp^3 fraction and residual stress in films decreased from Tersoff, REBO to AIREBO. The high residual compressive stress for three potentials was mainly determined by the high distortion of sp^3 C bond lengths, while the distorted sp^2 C bond lengths also contributed to it.
(2) Compared to Tersoff and REBO potentials, AIREBO potential was more suitable to describe the sp^3 and sp^2 structure, and also gave the reasonable residual stress, hybridization and density values.
(3) The difference in hybridization structures was related with the conjugation effect in these three potentials, in which the AIREBO accurately handled this overbinding of specific bonding configurations. On the other hand, the density in the film using AIREBO potential was evaluated by introducing the long-range LJ interaction, which was significant to accurately describe the nonbonded

structure of a-C film. However, in order to accurately evaluate the residual stress of a-C films, both LJ and torsion terms were required to be considered simultaneously.
(4) Comparing with the atom-by-atom deposition method, the a-C film fabricated by liquid-quenching method with AIREBO potential had similar structure, suggesting that the simulation based on AIREBO was independent on the processing method.

References

[1] J. Robertson, Diamond-like amorphous carbon, Mater. Sci. Eng. R 37 (4–6) (2002) 129–281.
[2] L. Zhang, X. Wei, Y. Lin, F. Wang, A ternary phase diagram for amorphous carbon, Carbon 94 (2015) 202–213.
[3] J. Huang, L. Wang, B. Liu, S. Wan, Q. Xue, In vitro evaluation of the tribological response of Mo-Doped graphite-like carbon film in different biological media, ACS Appl. Mater. Interfaces 7 (4) (2015) 2772–2783.
[4] N. Paik, Raman and XPS studies of DLC films prepared by a magnetron sputter-type negative ion source, Surf. Coat. Tech. 200 (7) (2005) 2170–2174.
[5] G. Speranza, N. Laidani, Measurement of the relative abundance of sp2 and sp3 hybridised atoms in carbon-based materials by XPS: a critical approach. Part II, Diamond Relat. Mater. 13 (3) (2004) 451–458.
[6] D. Galvan, Y.T. Pei, J.Th.M. De Hosson, A. Cavaleiro, Determination of the sp3C content of a-C films through EELS analysis in the TEM, Surf. Coat. Technol. 200 (1–4) (2005) 739–743.
[7] A. Dorner-Reisel, L. Kübler, G. Irmer, G. Reisel, S. Schöps, V. Klemm, E. Müller, Characterisation of nitrogen modified diamond-like carbon films deposited by radio-frequency plasma enhanced chemical vapour deposition, Diamond Relat. Mater. 14 (3–7) (2005) 1073–1077.
[8] B. Zheng, W.T. Zheng, K. Zhang, Q.B. Wen, J.Q. Zhu, S.H. Meng, X.D. He, J.C. Han, First-principle study of nitrogen incorporation in amorphous carbon, Carbon 44 (5) (2006) 962–968.
[9] D.G. McCulloch, D.R. McKenzie, C.M. Goringe, Ab initio simulations of the structure of amorphous carbon, Phys. Rev. B 61 (3) (2000) 2349–2355.
[10] X. Li, P. Ke, H. Zheng, A. Wang, Structure properties and growth evolution of diamond-like carbon films with different incident energies: a molecular dynamics study, Appl. Surf. Sci. 273 (2013) 670–675.
[11] S.J. Stuart, M.T. Knippenberg, O. Kum, P.S. Krstic, Simulation of amorphous carbon with a bond-order potential, Phys. Scr. T124 (2006) 58–64.
[12] T.B. Ma, L.F. Wang, Y.Z. Hu, X. Li, Hui Wang, A shear localization mechanism for lubricity of amorphous carbon materials, Sci. Rep. 4 (2014) 3662-1-6.
[13] J. Tersoff, New empirical approach for the structure and energy of covalent systems, Phys. Rev. B 37 (12) (1988) 6991–7000.
[14] P. Erhart, K. Albe, Analytical potential for atomistic simulation of silicon, carbon, and silicon carbide, Phys. Rev. B 71 (2005) 035211-1-14.
[15] D.W. Brenner, O.A. Shenderova, J.A. Harrison, S.J. Stuart, B. Ni, S.B. Sinnott, A second-generation reactive empirical bond order (REBO) potential energy expression for hydrocarbons, J. Phys.: Condens. Matter. 14 (4) (2002) 783–802.
[16] S.J. Stuart, A.B. Tutein, J.A. Harrison, A reactive potential for hydrocarbons with

intermolecular interactions, J. Chem. Phys. 112 (14) (2000) 6472–6486.

[17] A.C.T. Van Duin, S. Dasgupta, F. Lorant, W.A. Goddard, ReaxFF: a reactive force field for hydrocarbons, J. Phys. Chem. A 105 (41) (2001) 9396–9409.

[18] N.A. Marks, Thin film deposition of tetrahedral amorphous carbon: a molecular dynamics study, Diamond Relat. Mater. 14 (8) (2005) 1223–1231.

[19] D. Zhang, M.R. Dutzer, T. Liang, A.F. Fonseca, Y. Wu, K.S. Walton, D.S. Sholl, A.H. Farmahini, S.K. Bhatia, S.B. Sinnott, Computational investigation on CO_2 adsorption in titanium carbide-derived carbons with residual titanium, Carbon 111 (2017) 741–751.

[20] M. Joe, M.W. Moon, J. Oh, K.H. Lee, K.R. Lee, Molecular dynamics simulation study of the growth of a rough amorphous carbon film by the grazing incidence of energetic carbon atoms, Carbon 50 (2012) 404–410.

[21] T.B. Ma, Y.Z. Hu, H. Wang, X. Li, Microstructural and stress properties of ultrathin diamondlike carbon films during growth: molecular dynamics simulations, Phys. Rev. B 75 (2007) 035425-1-8.

[22] S. Plimpton, Fast parallel algorithms for short-range molecular dynamics, J. Comp. Phys. 117 (1) (1995) 1–19.

[23] H.J.C. Berendsen, J.P.M. Postma, W.F. van Gunsteren, A. DiNola, J.R. Haak, Molecular dynamics with coupling to an external bath, J. Chem. Phys. 81 (8) (1984) 3684–3690.

[24] D.R. McKenzie, D. Muller, B.A. Pailthorpe, Compressive stress induced formation of thin film tetrahedral amorphous carbon, Phys. Rev. Lett. 67 (1991) 773–776.

[25] N.A. Marks, Evidence for subpicosecond thermal spikes in the formation of tetrahedral amorphous carbon, Phys. Rev. B 56 (1997) 2441–2446.

[26] P.J. Fallon, V.S. Veerasamy, C.A. Davis, J. Robertson, G.A.J. Amaratunga, W.I. Milne, J. Koskinen, Properties of filtered-ion-beam-deposited diamondlike carbon as a function of ion energy, Phys. Rev. B 48 (1993) 4777–4782.

[27] K.J. Koivusaari, T.T. Rantala, S. Leppävuori, Calculated electronic density of states and structural properties of tetrahedral amorphous carbon, Diamond Relat. Mater. 9 (3–6) (2000) 736–740.

[28] S. Kaciulis, Spectroscopy of carbon: from diamond to nitride films, Surf. Interface Anal. 44 (2012) 1155–1161.

[29] A. Fujimoto, Y. Yamada, M. Koinuma, S. Sato, Origin of sp^3 C peaks in C1s photoelectron spectra of carbon materials, Anal. Chem. 88 (2016) 6110–6114.

[30] J. Vetter, 60 years of DLC coatings: historical highlights and technical review of cathodic arc processes to synthesize various DLC types, and their evolution for industrial applications, Surf. Coat. Technol. 257 (2014) 213–240.

[31] G.C. Abell, Empirical chemical pseudopotential theory of molecular and metallic bonding, Phys. Re. B 31 (1985) 6184–6196.

[32] D.W. Brenner, Empirical potential for hydrocarbon for use in simulating the chemical vapor deposition of diamond films, Phys. Rev. B 42 (15) (1990) 9458–9471.

[33] H.U. Jäger, K. Albe, Molecular-dynamics simulation of steady-state growth of ion-deposited tetrahedral amorphous carbon films, J. Appl. Phys. 88 (2) (2000) 1129–1135.

[34] L. Li, M. Xu, W. Song, A. Ovcharenko, G. Zhang, D. Jia, The effect of empirical potential functions on modeling of amorphous carbon using molecular dynamics method, Appl. Surf. Sci. 286 (2013) 287–297.